Dynamic wavefront shaping with an acousto-optic lens for laser scanning microscopy

George Konstantinou,[1,3] Paul A. Kirkby,[1,3] Geoffrey J. Evans,[1] K. M. Naga Srinivas Nadella,[1] Victoria A. Griffiths,[1] John E. Mitchell[2] and R. Angus Silver[1*]

[1]*Department of Neuroscience, Physiology and Pharmacology, University College London, Gower Street, London WC1E 6BT, UK*
[2]*Department of Electronic and Electrical Engineering, University College London, Gower Street, London WC1E 6BT, UK*
[3]*These authors contributed equally*
a.silver@ucl.ac.uk

Abstract: Acousto-optic deflectors (AODs) arranged in series and driven with linearly chirped frequencies can rapidly focus and tilt optical wavefronts, enabling high-speed 3D random access microscopy. Non-linearly chirped acoustic drive frequencies can also be used to shape the optical wavefront allowing a range of higher-order aberrations to be generated. However, to date, wavefront shaping with AODs has been achieved by using single laser pulses for strobed illumination to 'freeze' the moving acoustic wavefront, limiting voxel acquisition rates. Here we show that dynamic wavefront shaping can be achieved by applying non-linear drive frequencies to a pair of AODs with counter-propagating acoustic waves, which comprise a cylindrical acousto-optic lens (AOL). Using a cylindrical AOL we demonstrate high-speed continuous axial line scanning and the first experimental AOL-based correction of a cylindrical lens aberration at 30 kHz, accurate to $1/35^{\text{th}}$ of a wave at 800 nm. Furthermore, we develop a model to show how spherical aberration, which is the major aberration in AOL-based remote-focusing systems, can be partially or fully corrected with AOLs consisting of four or six AODs, respectively.

OCIS codes: (180.5810) Scanning microscopy; (010.1080) Active or adaptive optics; (110.0180) Microscopy ; (170.2520) Fluorescence microscopy; (170.6900) Three-dimensional microscopy; (230.1040) Acousto-optical devices.

References and links

1. A. Kaplan, N. Friedman, and N. Davidson, "Acousto-optic lens with very fast focus scanning," Opt. Lett. **26**(14), 1078–1080 (2001).
2. P. A. Kirkby, K. M. N. S. Nadella, and R. A. Silver, "A compact acousto-optic lens for 2D and 3D femtosecond based 2-photon microscopy," Opt. Express **18**(13), 13721–13745 (2010).
3. G. Duemani Reddy, K. Kelleher, R. Fink, and P. Saggau, "Three-dimensional random access multiphoton microscopy for functional imaging of neuronal activity," Nat. Neurosci. **11**(6), 713–720 (2008).
4. G. Katona, G. Szalay, P. Maák, A. Kaszás, M. Veress, D. Hillier, B. Chiovini, E. S. Vizi, B. Roska, and B. Rózsa, "Fast two-photon in vivo imaging with three-dimensional random-access scanning in large tissue volumes," Nat. Methods **9**(2), 201–208 (2012).

5. T. Fernández-Alfonso, K. M. N. S. Nadella, M. F. Iacaruso, B. Pichler, H. Roš, P. A. Kirkby, and R. A. Silver, "Monitoring synaptic and neuronal activity in 3D with synthetic and genetic indicators using a compact acousto-optic lens two-photon microscope," J. Neurosci. Methods **222**, 69–81 (2014).
6. F. Helmchen and W. Denk, "Deep tissue two-photon microscopy," Nat. Methods **2**(12), 932–940 (2005).
7. N. Friedman, A. Kaplan, and N. Davidson, "Acousto-optic scanning system with very fast nonlinear scans," Opt. Lett. **25**(24), 1762–1764 (2000).
8. P. A. Kirkby, K. M. N. S. Nadella, and R. A. Silver, "Methods and Apparatus to Control Acousto-Optic Deflectors (U.S. patent WO/2012/143702)," .
9. P. Bechtold, R. Hohenstein, and M. Schmidt, "Beam shaping and high-speed, cylinder-lens-free beam guiding using acousto-optical deflectors without additional compensation optics." Opt. Express **21**(12), 14627–14635 (2013).
10. W. Akemann, J.-F. Léger, C. Ventalon, B. Mathieu, S. Dieudonné, and L. Bourdieu, "Fast spatial beam shaping by acousto-optic diffraction for 3D non-linear microscopy," Opt. Express **23**(22), 28191-28205 (2015).
11. G. Y. Fan, H. Fujisaki, A. Miyawaki, R. K. Tsay, R. Y. Tsien, and M. H. Ellisman, "Video-rate scanning two-photon excitation fluorescence microscopy and ratio imaging with cameleons," Biophys. J. **76**(5), 2412–2420 (1999).
12. X. Chen, U. Leischner, Z. Varga, H. Jia, D. Deca, N. L. Rochefort, and A. Konnerth, "LOTOS-based two-photon calcium imaging of dendritic spines in vivo," Nat. Protoc. **7**(10), 1818–1829 (2012).
13. J. Xu and R. Stroud, *Acousto-Optic Devices: Principles, Design, and Applications* (Wiley, 1992).
14. J. W. Goodman, *Introduction to Fourier Optics* (McGraw-Hill, 1996).
15. E. J. Botcherby, C. W. Smith, M. M. Kohl, D. Débarre, M. J. Booth, R. Juškaitis, O. Paulsen, and T. Wilson, "Aberration-free three-dimensional multiphoton imaging of neuronal activity at kHz rates," Proc. Natl. Acad. Sci. U. S. A. **109**(8), 2919–2924 (2012).
16. N. Collings, T. Davey, J. Christmas, D. Chu, and B. Crossland, "The Applications and Technology of Phase-Only Liquid Crystal on Silicon Devices," J. Disp. Technol. **7**(3), 112–119 (2011).
17. P.-Y. Madec, "Overview of Deformable Mirror Technologies for Adaptive Optics," in "Imaging Appl. Opt. 2015," (OSA, Washington, D.C., 2015), AOTh2C.1.
18. "Meadowlark Optics," http://www.meadowlark.com.
19. "Boston Micro Machines Kilo S Deformable Mirror," http://www.bostonmicromachines.com.
20. T. G. Bifano and J. B. Stewart, "High-speed wavefront control using MEMS micromirrors," in M. T. Valley and M. A. Vorontsov, eds., "Opt. Photonics 2005," (International Society for Optics and Photonics, 2005), 58950–58959.
21. E. Chaigneau, A. J. Wright, S. P. Poland, J. M. Girkin, and R. A. Silver, "Impact of wavefront distortion and scattering on 2-photon microscopy in mammalian brain tissue," Opt. Express **19**(23), 22755–22774 (2011).
22. M. J. Booth, "Adaptive optics in microscopy." Philos. Trans. A. Math. Phys. Eng. Sci. **365**(1861), 2829–2843 (2007).
23. J. R. Moffitt, Y. R. Chemla, S. B. Smith, and C. Bustamante, "Recent Advances in Optical Tweezers," Annu. Rev. Biochem. **77**(1), 205–228 (2008).
24. P. S. Salter, A. Jesacher, H. Al-Wakeel, and M. Booth, "Laser microfabrication using adaptive optics: parallelization and aberration correction," in "Imaging Appl. Opt.", (OSA, Washington, D.C., 2011), AMC5.
25. Y.-C. Li, L.-C. Cheng, C.-Y. Chang, C.-H. Lien, P. J. Campagnola, and S.-J. Chen, "Fast multiphoton microfabrication of freeform polymer microstructures by spatiotemporal focusing and patterned excitation," Opt. Express **20**(17), 19030–19038 (2012).
26. E. Walker, A. Dvornikov, K. Coblentz, S. Esener, and P. Rentzepis, "Toward terabyte two-photon 3D disk," Opt. Express **15**(19), 12264–12276 (2007).
27. F. K. Fatemi, M. Bashkansky, and Z. Dutton, "Dynamic high-speed spatial manipulation of cold atoms using acousto-optic and spatial light modulation," Opt. Express **15**(6), 3589-3596 (2007).
28. T. Čižmár, H. I. C. Dalgarno, P. C. Ashok, F. J. Gunn-Moore, and K. Dholakia, "Optical aberration compensation in a multiplexed optical trapping system," J. Opt. **13**(4), 44008-44009 (2011).
29. T. J. Gould, D. Burke, J. Bewersdorf, and M. J. Booth, "Adaptive optics enables 3D STED microscopy in aberrating specimens," Opt. Express **20**(19), 20998-21009 (2012).
30. B. Judkewitz, Y. M. Wang, R. Horstmeyer, A. Mathy, and C. Yang, "Speckle-scale focusing in the diffusive regime with time-reversal of variance-encoded light (TROVE)," Nat. Photonics **7**(4), 300–305 (2013).

1. Introduction

Acousto-optic lenses (AOLs) allow rapid, inertia-free focusing and scanning of an optical beam. Originally developed for cold atom research [1], AOLs have found applications in high-speed, 3D, two-photon microscopes [2–5] to monitor signalling deep within the scattering tissue of the brain [6]. AOLs are well suited for this application because they enable 3D random-access

multi-photon (RAMP) microscopy, which allows spatially distributed points of interest to be monitored at rates of 30–50 kHz [3].

AOLs use pairs of acousto-optic deflectors (AODs) to focus and deflect an optical beam (Fig. 1(a)). The AODs in each pair are oppositely orientated such that their acoustic waves are counter-propagating in space. A single pair of AODs can form a cylindrical AOL and an orthogonal pair of cylindrical AOLs form a spherical AOL. The names are analogous to cylindrical and spherical lenses. Focusing is achieved by driving the transducers of the AODs with linearly-chirped frequencies, while beam steering is achieved by offsetting the frequency [1].

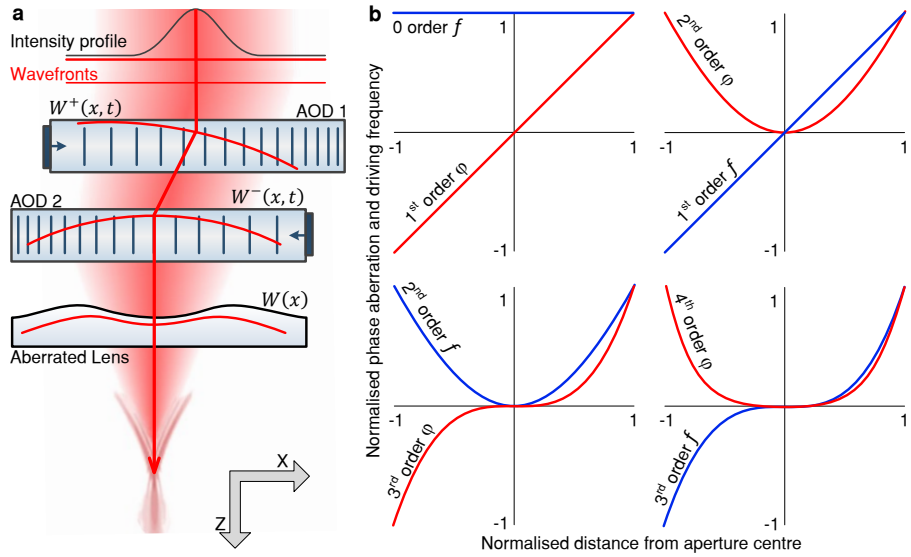

Fig. 1. Operating principle of an acousto-optic lens. (a) Schematic diagram of light propagation through a cylindrical AOL, which comprises two acousto-optic deflectors (AODs) with counter-propagating acoustic waves, together with an aberrated lens. The optical wavefront at each stage is indicated by the red lines and the acoustic waves are indicted by the vertical dark-blue lines within AOD1 and AOD2. (b) Relationship between phase ($\phi = 2\pi x^n$) and frequency ($f = nVx^{n-1}$) shown across the aperture for $n \in \{1,2,3,4\}$, where the position is denoted by x and the acoustic velocity by V.

Two AODs with counter-propagating acoustic waves can work together to control the (2D) focal position. In Fig. 1(a), a linearly chirped acoustic wave is shown across the first AOD with descending frequency. This results in the diffracted optical beam having a parabolic wavefront (Fig. 1(b), top right). However, the wavefront leaving the first AOD (and hence the focal spot) will move laterally at the same speed as the acoustic wave. The counter-propagating acoustic wave of the second AOD is therefore necessary to prevent the focus drifting with the acoustic wave of the first AOD. Each AOD contributes half of the total curvature of the outgoing optical beam.

The arrangement of AODs in a spherical AOL enables discontinuous RAMP point measurements over a 3D region of space and also repeated continuous line scanning in a lateral direction (xy-plane) [2–4]. Changing focus (z) is discontinuous because it requires the new acoustic ramp with a different slope to propagate across the AOD aperture. This prevents continuous axial line scanning, limiting the speed at which imaging can be performed in planes with varying z.

Early work [1, 7] demonstrated fast axial oscillatory scanning using sinusoidally-modulated frequency drives. However, the speed was limited due to unwanted aberrations caused by the

non-linear drives, which grew with the frequency of the sinusoidal-modulation. Recent theoretical progress based on expressing non-linear drive frequencies as power series has revealed that each coefficient has a direct physical interpretation, enabling aberration-free, constant-velocity axial line scanning and targeted aberration generation [8]. However, implementing continuous non-linearly chirped AOL drive is complicated because the drive frequency of each AOD must be calculated to account for the propagation of the acoustic waves across the AODs.

An alternative approach for implementing wavefront shaping in AODs, is to use time-locked single laser pulses for strobed illumination to 'freeze' the moving acoustic waves. Because the speed of light is much faster than that of acoustic waves in AODs, each optical pulse effectively encounters a fixed diffraction grating at each AOD. The pulsed illumination method has been used to generate several types of optical aberration using two AODs, oriented in x- and y-directions respectively, and could be extended to correct for optical aberrations during RAMP microscopy [9, 10].

Whilst the single-pulse strobing method avoids the complication of acoustic waves propagating across the AODs [7], it requires a pause between each pulse of at least an entire AOD fill time. This limits the pixel acquisition rate to the AOD fill rate because each pixel corresponds to a single laser pulse. Higher speeds can be achieved with smaller crystals but this comes at the cost of a lower time-bandwidth product. For example a diffraction limited 512×512 pixel image would require large AOD apertures (or more precisely large time-bandwidth products) restricting the temporal resolution to 30–50 kHz.

A problem with the low rates of voxel acquisition associated with the single-pulse stroboscopic method is that building up full-frame images takes seconds, and z-stacks can take minutes which is problematic for *in vivo* imaging, particularly when there is movement. This contrasts with 2D resonance galvanometer and AOL-based imaging which can achieve line (typically 512 pixels per line) acquisition rates of 10–20 kHz and full-frame imaging at 20–40 Hz [11, 12]. Thus, these are over 100 times faster than the single-pulse stroboscopic method.

To address these limitations we have developed a high-speed *field-programmable gate array* (FPGA)-based control system that can generate a range of precise, non-linear drive frequencies, used to shape the optical wavefront [8]. By using counter-propagating non-linearly chirped acoustic waves in a cylindrical AOL, we demonstrate continuous line scanning of a laser beam in both the lateral and axial directions. Moreover, we provide the first experimental demonstration of AOL-based correction of fixed aberrations introduced by a cylindrical lens and show with modelling how spherical aberration could be corrected by an AOL consisting of six AODs. These features can be combined to make a random access pointing and scanning (RAPS) microscope capable of low-order aberration correction at over 30 kHz.

2. Methods

2.1. Derivation of drive equations

The parabolic optical wavefront required for focusing is just one of many wavefronts that can potentially be generated by an AOL. To generate arbitrary optical wavefronts with a cylindrical or spherical AOL it was necessary to derive the general relationship between the phase of the acoustic waves and the optical wavefront leaving the AOL. When discussing aberrations in the context of a cylindrical AOL we are restricted to 2D and refer to the 2D aberrations by terms such as coma-like and spherical-like since these are their closest 3D counterparts.

The phase of the optical wave is controlled by diffraction at each of the two AODs via the addition (or subtraction) of the acoustic phases [13]. Since the AODs are taken to be thin and the acoustic waves propagate with speed V, we let $W^+(t-x/V)$ and $W^-(t+x/V)$ represent a pair of acoustic waves counter-propagating across the first and second AODs respectively. W^+ is travelling in the positive x-direction and W^- in the negative x-direction (Fig. 1(a)). We

let $U_{\text{in}}(x)$ represent our incident optical field, which typically has a Gaussian amplitude profile with approximately constant phase. In the case that the AODs are operating in the +1 mode, assuming that the optical beam is not truncated by the aperture and the diffraction efficiency of the AODs is close to 100% across the whole aperture, the outgoing optical field $U(x,t)$ will satisfy

$$U(t,x) \propto U_{\text{in}}(x) W^{+}(t-x/V) W^{-}(t+x/V) \tag{1}$$

For the alternative case that the AODs are operating in the -1 mode, $W^{+}(t-x/V)$ and $W^{-}(t+x/V)$ are replaced by their complex conjugates. Note also that for simplicity these equations assume the (axial) distance between each AOD to be zero. At time $t=0$, the counter-propagating acoustic waves are both centred on their AODs at $x=0$.

To proceed, we expand the phase modulation of the acoustic wave functions W^{+} and W^{-} in power series up to the N^{th} order:

$$\begin{aligned} W^{+}(t-x/V) &= W_0 \exp\left(2\pi i\left\{f(t-x/V)+\sum_{n=1}^{N} P_n^{+}\left(\frac{t-x/V}{\tau/2}\right)^n\right\}\right) \\ W^{-}(t+x/V) &= W_0 \exp\left(2\pi i\left\{f(t+x/V)+\sum_{n=1}^{N} P_n^{-}\left(\frac{t+x/V}{\tau/2}\right)^n\right\}\right) \end{aligned} \tag{2}$$

where W_0 is the amplitude of the acoustic waves, f is the centre frequency of the AODs and τ is the AOD fill time. The fill time is related to the AOD aperture width L by $\tau = L/V$. Thus the magnitude of each coefficient $P_n^{\pm}$ equals the number of waves of phase aberration for each order at the edges of the AOD aperture at $t=0$. For comparison, an optical ray passing through the centre ($x=0$) of the first and second AODs at $t=0$ encounters the frequencies $f+2P_1^{+}/\tau$ and $f+2P_1^{-}/\tau$ respectively (it is unaffected by the non-linear components $P_{n>1}^{\pm}$).

This theoretical treatment ignores real-world time and space constraints. Spatially, our waves are constrained by the AOD apertures such that Eq. (2) holds only for $|x| \leq L/2$ and the optical and acoustic waves are zero outside this region. Temporally, frequency ramps are periodically reset either to remain within the bandwidth of the AODs or to change the scan trajectory. The duration of a frequency ramp is given by the sum of the fill time and the data collection time T. The data collection time is the period beginning when the AODs are filled and ending at the end of the ramp; this is the period when the AOL is able to produce a well-formed unaberrated point spread function (PSF). The time $t=0$ is taken to be $\tau + T/2$ after the start of the frequency ramp. Thus our time variable is constrained to $-\tau - T/2 < t \leq T/2$, resetting as one ramp ends and a new one begins. These constraints do not affect the substance of Eq. (2), which applies individually to each frequency ramp.

Substituting Eq. (2) into Eq. (1) and taking U_{in} to have constant phase, we arrived at an expression for the phase of the outgoing optical wave, ϕ:

$$\phi = 4\pi f t + 2\pi \sum_{n=1}^{N}\left(P_n^{+}\left[\frac{t-x/V}{\tau/2}\right]^n + P_n^{-}\left[\frac{t+x/V}{\tau/2}\right]^n\right) \tag{3}$$

where the first term is a global phase that we can ignore. We identified how different terms in Eq. (3) combine to produce particular phase profiles of interest. Under our paraxial assumptions, these phase profiles can be converted into wavefronts by dividing the profile by 2π and multiplying by λ. Our key theoretical predictions are summarised in Table 1, which are valid for both AODs operating in the +1 mode (sign changes are needed for -1 mode). The relation between acoustic drive frequency $F(t)$ and acoustic phase Φ is given by:

$$F(t) = \frac{1}{2\pi}\frac{\partial \Phi}{\partial t} \tag{4}$$

Table 1. Summary of theoretical results.

n	P_n^+	P_n^-	Optical wavefront out	Physical interpretation
1	A	A	$z = \text{const}$	no net effect
1	A	$-A$	$z = \frac{-4\lambda A}{\tau V}x$	lateral shift: $\frac{4\lambda A}{\tau V}$ rad
2	B	B	$z = \frac{8\lambda B}{\tau^2 V^2}x^2$	axial shift: $\frac{16\lambda B}{\tau^2 V^2}$ dioptres
2	B	$-B$	$z = \frac{-16\lambda B}{\tau^2 V}tx$	lateral velocity: $\frac{16\lambda B}{\tau^2 V}$ rad/s
3	C	C	$z = \frac{48\lambda C}{\tau^3 V^2}tx^2$	axial velocity: $\frac{96\lambda C}{\tau^3 V^2}$ dioptres/s
3	C	$-C$	$z = \frac{-48\lambda C}{\tau^3 V}t^2x + \frac{-16\lambda C}{\tau^3 V^3}x^3$	lateral acceleration + coma-like aberration
4	D	D	$z = \frac{192\lambda D}{\tau^4 V^2}t^2x^2 + \frac{32\lambda D}{\tau^4 V^4}x^4$	axial acceleration + spherical-like aberration

The different phase components listed in Table 1 are independent, so they can be added to produce linear combinations. As noted in the Table, a pair of equal-amplitude same-sign third-order ($n = 3$) phase components produce a continuous axial scan. However, if the third-order component was present across only one AOD, a coma-like aberration would be produced. It is the destructive interference between the two counter-propagating third-order phase components that removes the aberration, leaving only a time-varying parabolic wavefront. This overcomes the serious issue of unwanted aberrations, that was highlighted in earlier work [7]. Similarly, same-sign, fourth-order phase components interfere to remove coma-like aberration, producing a focus that accelerates in the z-direction and produces a fixed spherical-like aberration. In the remainder of the paper, we explore the third and fourth-orders, because continuous axial line scanning and the correction of spherical-like aberration are of significant interest and have not previously been demonstrated experimentally with an AOL.

2.2. Fourier modelling of cylindrical AOL in 2D

To theoretically compute the 2D optical intensity pattern observed in the focal region, we used standard 1D angular spectrum Fourier optics techniques [14]. AODs were modelled as phase shifts, in accordance with Eq. (1). Monochromatic light was used since chromatic aberration was small in the regions of interest (for details on chromatic effects see [2]). The optical phase shift introduced by a cylindrical lens immediately following the AOL was described by the complex expression

$$W(x) = \exp\left(2\pi i \sum_{n=1}^{N} P_n \left[\frac{x}{L/2}\right]^n\right) \tag{5}$$

The phase of the optical wave after the lens is then given by the product of Eqs. (1) and (5): $U(t,x)W(x)$. The xz-intensity planes were then created in the focal region of the lens by propagating the angular spectrum of this optical field over a range of z-positions [14]. The wavefront imposed on the optical beam by the counter-propagating acoustic waves of the AOL is time dependent. To account for time, we repeated the procedure over a typical range of 2–20 μs. The same approach was used to calculate the time dependence of the focal position.

Once the optical field had been calculated over the focal region, it was related to intensity by squaring and to two-photon excitation by squaring again. For the images acquired using the camera or the photodiode, pixel brightness was proportional to intensity. In a two-photon AOL microscope, pixel brightness would be proportional to intensity squared.

2.3. Control system and experimental setup

To test our theoretical predictions that AOLs can be used for continuous axial line scanning and 2D-spherical-like aberration correction using non-linearly chirped acoustic drive frequencies, we built the following experimental setup (Fig. 2).

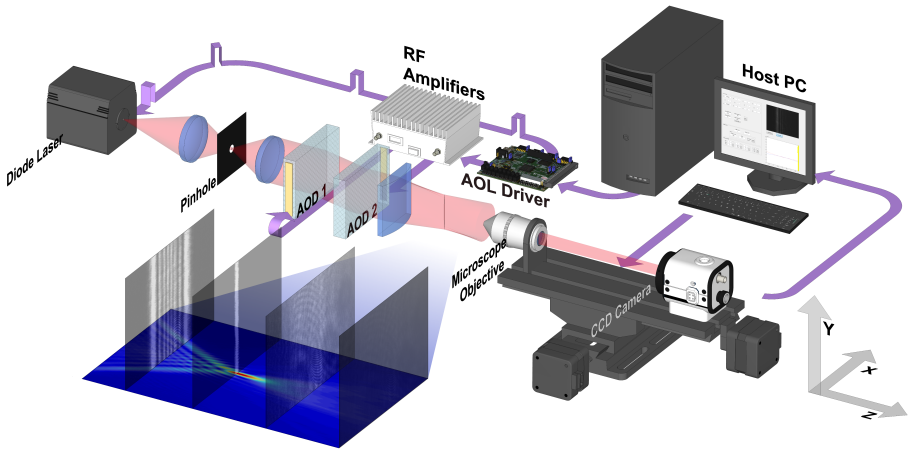

Fig. 2. Schematic diagram of experimental setup. From left to right: the pulsed diode laser, was spatially filtered with a pinhole and projected through the two AODs with counter-propagating acoustic waves, which were generated by the FPGA control system and radio frequency (RF) amplifiers, under the control of the host PC. The light was focused by a fixed cylindrical lens. The microscope objective was used to project an image of a plane in the focal region onto a CCD camera. Both the objective and the camera were mounted on a motorized stage enabling a z-stack of the focal region to be imaged.

Light from a 100 mW, 785 nm, diode laser (Ondax TO-785-PLR80) was spatially filtered with a 5 μm pinhole and then collimated by a 60 mm focal length achromatic lens to form an approximately Gaussian beam of 13.2 mm FWHM (full width at half maximum) truncated at 25 mm diameter. A quarter-wave plate was used to convert the polarization to right-hand circular. The light was then diffracted by the first AOD (-1 mode), which was a custom designed 18 mm aperture on-axis TeO_2 crystal with a 38 MHz center frequency for 800 nm optical wavelength (Gooch & Housego, bandwidth of 20 MHz and time-bandwidth product of 500). The polarization was then changed again to linear by a quarter-wave plate, and the unwanted zero order filtered out by a linear polarizer. Prior to entering the second AOD, the polarization was changed to right-hand circular by another quarter-wave plate. Finally, the diffracted beam leaving the second AOD (-1 mode again) was focused by a cylindrical lens (focal lengths used: 50 mm, 75 mm or 100 mm).

The control system, which generated precise radio frequency (RF) drive signals as functions of time, was developed on a Virtex 5 board (Xilinx), which implemented Eq. (2). Digital waveforms were then passed to a 14 bit, 300 MSPS DAC (Texas Instruments) and the RF signals amplified with 20–60 MHz bandwidth, 12 W, Class B (ISOMET) amplifiers. Our system produced continuous RF frequency ramps defined by third-order polynomials in time (fourth-order

in phase), with a quantization step of 0.064 Hz in frequency and 3.33 ns in time. The ramps were reset at intervals of $\tau + T$. A MATLAB script was used to synchronize the RF control system and the diode laser such that a 1 μs optical pulse was triggered at $t = -0.5$ μs or offset to correspond to an earlier (Fig. 3(a,d)) or later (Fig. 3(c,f)) instant of the frequency ramps.

A 20$\times$ microscope objective (NA = 0.75) projected the light onto the CCD of a near-infrared sensitive camera (Hamamatsu C3077, 752$\times$482 pixels, 11.5 μm pixel size). The camera was at a sufficient distance to be in the far-field limit, so a tube lens was not needed. Both were mounted on a computer-controlled motorized stage (Luigs & Neumann). In order to image the optical focus, the camera and microscope objective assembly was moved incrementally in the z-direction by the motorized stage. The focus was visualized as a 2D pseudocolour plot by capturing a sequence of CCD images over a range of z-positions, and integrating the image over the y-axis (Fig. 2).

3. Results

3.1. Axial scanning

We tested our theoretical prediction that a cylindrical AOL could scan the focal-position continuously in the z-direction by driving the two AODs with same-sign third-order phase components to produce a time-varying parabolic wavefront (Fig. 3(a–c)). The shape of the focus was similar at three different times (Fig. 3(d–f)) as the wavefront evolved (Fig. 3(a–c)). Moreover, the focal position shifted in z with the predicted constant velocity. By illuminating the AOL continuously for 14 μs (from 30–44 μs after ramp start), we monitored the intensity of the focus continuously as a scan progressed and found it to be approximately constant along the 4 mm axial range. This confirmed the prediction that no substantial aberrations are introduced by axial scanning (Fig. 3(g)).

To test whether we could extend this result from purely axial scanning to simultaneous axial and lateral scanning (xz-scanning), we added opposite-sign second-order phase components which introduce a lateral velocity (Table 1). Increasing the magnitude of the second-order components increased the lateral scanning speed (Fig. 3(h–i)). There was greater variation of the intensity along the scan, with this being most pronounced for fast lateral scanning (Fig. 3(i)). As there was no apparent effect on the shape of focus, these effects are likely to result from variations in AOL transmission efficiency as previously noted for purely lateral scanning at planes above and below the natural focal plane of the lens [2].

In Fig. 3(h,i), small intensity variations can be seen in the form of vertical bands starting from low spatial frequency on the left and becoming higher on the right. This is consistent with an optical interference effect between the imperfectly anti-reflection coated cylindrical lens and a flat surface, analogous to Newton's Rings and unrelated to the AODs.

We next explored how changes in the magnitude of the third-order component affected the axial scanning speed and thus the axial-range covered during a 14 μs scan. For the cylindrical AOL and a plano-convex 75 mm cylindrical lens combination (Fig. 3(j)), we identified the focal position by the peak intensity, and found agreement with our theoretical predictions over the duration of the scan for three different values for the third-order phase components. The relationship between the focal position and time gave scan speeds of 209 ms^{-1} and 418 ms^{-1} for 5 and 10 waves of third-order phase, respectively. The intersection of the scans produced by different magnitude third-order components marks the time $t = 0$, programmed to be 32.9 μs after the start of the ramp, when the cubic-phase in both AODs are perfectly anti-symmetric: at that instant, the cubic phases interfere destructively, producing a planar wavefront and the focal length is simply that of the cylindrical lens.

These results demonstrate that the synthesis of non-linearly chirped RF drives using our custom-designed FPGA AOL control system and the conversion to acoustic waves by the AODs

are sufficiently precise to generate axial scans without generating unwanted aberrations. More generally, we have shown that *xz*-scans of arbitrary gradient and scan speed can be produced by using linear combinations of the phase components for axial and lateral scanning.

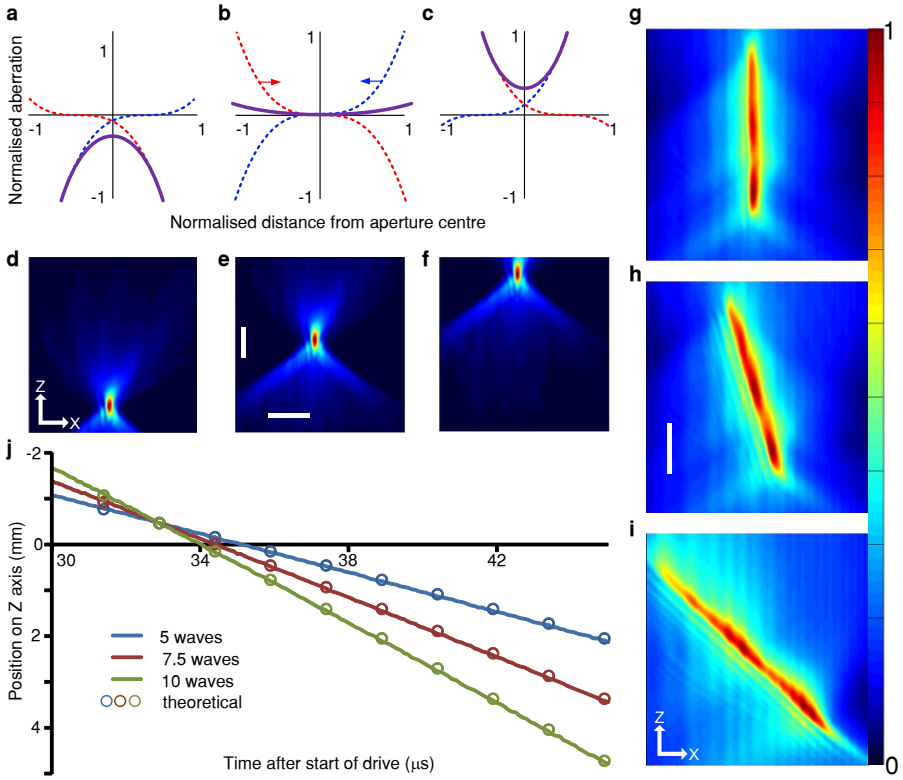

Fig. 3. Continuous axial line scanning. (a–c) Relationships between the phases of the counter-propagating acoustic waves of a cylindrical AOL (AOD1, blue; AOD2, red) at different instants in time (respectively 30, 35, 40 μs after ramp start). The resulting phase imposed on the optical beam is shown in purple. (d–f) Images of 1 μs light pulses at the times corresponding to (a–c) respectively. (g) Trajectory of focus during a purely axial scan produced using the third-order phase components shown in (a–c) made by imaging 14 μs duration laser illumination. (h) Similar to (g) but with second-order phase components which introduce lateral velocity. (i) Similar to (h) but with faster lateral velocity. (j) Relationship between axial displacement and time after the start of drive of the scan, for three different magnitudes of third-order phase components (P_3 in Table 1). The solid lines show the measured peak intensity and the circles show the theoretically expected trajectory for each case. Scales (d–i): horizontal scale bar is 50 μm, vertical bar is 1 mm.

3.2. Aberration correction

3.2.1. Spherical-like aberration correction

We examined how fourth-order phase components affect the focus, since they are expected to introduce 2D-spherical-like aberration. Our interest in spherical-like aberration derives from the fact that systems that use remote imaging (such as an AOL microscope) suffer from spherical aberration when focusing far away from the natural focal plane of the objective lens. The axial range of our AOLs and others reported in the literature exceed 1 mm. However, the magnitude

of the aberrations far from the natural focal plane limit the utility of the full axial range [4]. The ability to correct for spherical aberrations, enable higher quality imaging over larger axial ranges.

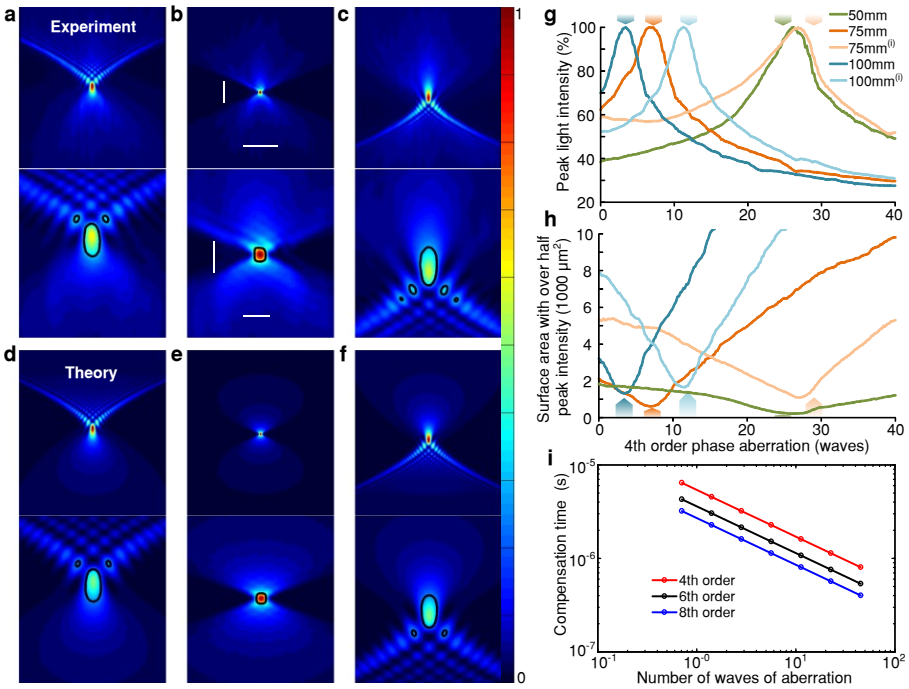

Fig. 4. Correction of 2D-spherical-like aberration. (a) Experimentally measured focus exhibiting spherical-like aberration. (b) Same as (a) but with -3.3 waves of fourth-order phase added per AOD ($P_4^{\pm} = -3.3$ in Table 1). (c) Same as (b) but with -6.6 waves per AOD (see Visualization 1 - 50 mm lens, Visualization 2 - 75 mm lens, Visualization 3 - 75 mm lens inverted, Visualization 4 - 100 mm lens, Visualization 5 - 100 mm lens inverted). (d–f) Theoretical focus corresponding to (a–c), calculated with a the model described in Section 2.2. (a–f) Top panels: colour scales normalised to the peak intensity in each panel; scale bars: horizontal 50 μm, vertical 1 mm. Bottom panels: magnified and normalised to the peak intensity across the three scenarios; scale bars: horizontal 10 μm, vertical 0.5 mm. (g,h) Normalised peak intensity and area with an intensity over the half maximum both plotted respectively against the (absolute) sum of the fourth-order phase components of the acoustic waves. Phase aberration discretized in 0.2 wave steps. The arrowheads mark the theoretical prediction of optimal correction for each of three forward-facing plano-convex lenses and two inverted lenses (normal plano-convex lenses used backwards) denoted by $^{(i)}$. (a–h) are all at $t = 0$, experimentally set to be 32.9 μs after each ramp start. (i) Calculated duration of aberration compensation shown for fourth, sixth and eighth-order phase components as a function of the number of waves being compensated. Logarithmic plot with gradient of -1/2 indicates inverse square-root dependence.

Same-sign, fourth-order phase components introduce spherical-like aberration together with axial acceleration of the focal position (Table. 1). To test whether the AOL could correct for a defined amount of spherical-like aberration, we introduced +6.6 waves of spherical-like aberration into the optical beam with a plano-convex lens. When the AOL generated flat optical wavefronts, the 75 mm cylindrical lens produced a focus with spherical-like aberration (Fig. 4(a)). When -6.6 waves of spherical-like aberration were introduced by driving each

AOD in the AOL with -3.3 waves of fourth-order phase, the focus became sharp and symmetrical (Fig. 4(b)), indicating the lens' aberration had been cancelled out.

Visualizations of the corrected focus at higher magnification (Fig. 4(b), lower panel) revealed that the size of the high-intensity region decreased and the peak intensity increased compared to the focus obtained without correction (Fig. 4(a), lower panel). When the magnitude of the fourth-order phase component was doubled to -6.6 waves on each AOD, the focal pattern became inverted, with the characteristic interference patterns appearing distal to the lens (Fig. 4(c)). The experimentally measured foci closely match our Fourier optics model of the AOL and cylindrical lens with 0, -3.3 and -6.6 waves of fourth-order phase per AOD (Fig. 4(d–f)) even at high magnification (Fig. 4(d–f) lower panels).

To further examine how well the cylindrical AOL could correct for spherical-like aberration, we repeated the experiment using cylindrical lenses with different focal lengths (50 mm and 100 mm). To quantify changes in the focus, we measured the peak intensity and the cross-sectional area at over half the maximum intensity (see contours on lower parts of Fig. 4(a–f)). The peak intensity depended sensitively on the amount of spherical-like aberration introduced by the AOL (Fig. 4(g)). For three different lenses of focal length 50, 75 and 100 mm and two inverted cases, we observed maxima in the range -26.2 to -3.4 waves of aberration for lenses, close to the values predicted with a Zemax geometric optical model (Fig. 4(g), arrowheads). Quantifying the focus by cross-sectional area above half-maximum intensity instead of peak intensity gave similar results, with the area minima coinciding with the peak intensity maxima (Fig. 4(g,h)).

3.2.2. Modelling aberration compensation time-dependence

AOLs are inherently discontinuous devices: time is required for the acoustic wave to travel across the aperture of the crystals, and the time-varying RF drive has to be reset periodically to keep it within the bandwidth of the AOD. For each period following a reset, there is only one time instant ($t = 0$) when the two counter-propagating waves exactly compensate the fixed aberration of the lens, each contributing half the required correction pattern. Therefore the calculated duration over which an aberration can be generated depends on how quickly the superposition pattern of the two counter-propagating acoustic waves changes.

To quantify the duration over which aberration correction can be performed and explore its dependence on the magnitude of correction, we used a range of differently aberrated lenses (Eq. (5) and Fig. 1) and calculated the temporal evolution of the outgoing optical field and the changing intensity pattern at the focus using the 1D angular spectrum Fourier method described in Section 2.2. The duration, shown in Fig. 4(i), is defined as the FWHM (in time) of the point (voxel) that reaches the greatest brightness. We used intensity squared as brightness since this is the relevant measure for two-photon imaging. Note that the correction time varies inversely with the order of the aberration and inversely with the square root of the magnitude of the aberration (for even powers). It is typically in the 1 to 10 μs range symmetrically about the optimum compensation time ($t = 0$), a length that is useful for pointing and raster scanning. The reason for the limited spherical aberration correction time at one position is that the focus is axially accelerating, consistent with the inverse square-root dependence on aberration magnitude.

These results demonstrate that spherical-like aberration of up to 26 waves can be corrected with an AOL for durations that are useful for imaging. They also show there is close agreement between the calculated aberration of the cylindrical lenses and the magnitude of the fourth-order phase components required for the AOL to achieve a perfect focus.

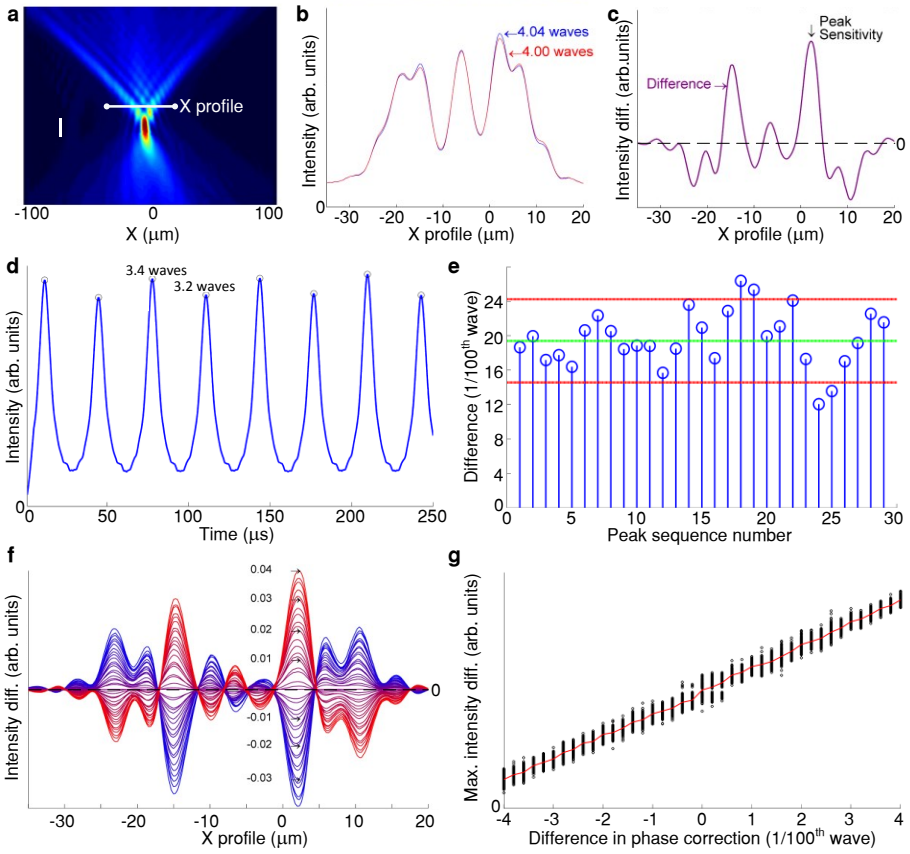

Fig. 5. Measurement of 2D-spherical-like aberration correction precision. (a) Profile of focus with 2D-spherical-like aberration introduced by driving the AODs of a cylindrical AOL with 4 waves of fourth-order phase ($P_4^{\pm} = 4$ in Table 1). Scale bar 0.5 mm. (b) Intensity profile across the horizontal line in (a), for $P_4 = 4$ and $P_4 = 4.04$ waves. (c) Difference in intensity profiles for $P_4 = 4$ and $P_4 = 4.04$ waves with arrow indicating the location of peak sensitivity. (d) Intensity at region of peak sensitivity for $P_4 = 3.4$ and $P_4 = 3.2$ waves measured at 30 kHz using a silicon detector and slit. (e) Differences in intensity between adjacent maxima normalised to the mean difference (green line) and scaled to units of waves of phase by aligning the mean with 0.2 waves. Red lines indicate ± 1 standard deviation. (f) Intensity difference profiles [cf. (c)] in steps of 0.002 waves from -0.04 waves of correction to $+0.04$ waves, integrated vertically over the CCD camera image. (g) Plot of 300 measured intensity differences against waves of fourth-order phase (black circles). Mean at each step shown by the red line.

3.2.3. Precision measurements

The ability to dynamically change the PSF by altering the aberrations introduced by the AOL, allowed us to test the speed and precision of AOL-based wavefront shaping with our experimental setup (Fig. 2). First we found a position in the *xz*-plane near the focus (Fig. 5(a–c)) of large intensity change with small changes in aberration, then replaced the camera with a 10 MHz bandwidth silicon photodiode (PDA36A, Thorlabs) behind a 5 μm slit at this most sensitive position.

We then used a high-speed sampling oscilloscope (Tektronix, MDO4104-6) to record intensity versus time as we toggled between $P_4 = 3.4$ and $P_4 = 3.2$ waves of aberration at 30 kHz

(Fig. 5(d,e)). Since we found that over small ranges of wavefront correction, intensity appeared to vary linearly with the number of waves of aberration correction, we modelled the intensity with a straight line plus Gaussian noise with mean zero and variance σ^2:

$$I_w = \beta w + \alpha + N\left(0, \sigma^2\right) \tag{6}$$

where w is the number of waves of aberration, and $N(\text{mean,variance})$ denotes Gaussian noise. α and β are unknown constants.

The difference of two random variables has variance equal to the sum of their respective variances, so intensity differences between the peaks will have the simple relation

$$I_{3.4} - I_{3.2} = 0.2\beta + N\left(0, 2\sigma^2\right) \tag{7}$$

We calculated the mean and estimated the standard deviation of the difference trace ($\sigma\sqrt{2}$) as shown by the green and red lines in Fig. 5(e), respectively. By noting the mean difference in intensity corresponded to 0.2 waves of aberration, we converted the estimated differential 15 kHz standard deviation into a number of waves of aberration. Our estimate of standard deviation of the differential was $1/25^{\text{th}}$ of a wave ($\sigma\sqrt{2}$ = 0.039 waves) implying that the standard deviation of intensity for each data point was $1/35^{\text{th}}$ of a wave (σ = 0.028 waves). We confirmed this by directly measuring the intensity noise when running the AOL repeatedly at 30 kHz at either 3.2 or 3.4 waves of aberration correction and using the same scaling factor to convert the intensity noise to precision of aberration control. In both cases the estimated precision was better than $1/35^{\text{th}}$ of a wave.

The fluctuations in our AOL measurements are likely to be caused by atmospheric turbulence, shot noise and amplifier and detector noise. We expected that the fluctuations could be averaged out and therefore examined how AOL precision was affected by integrating over many laser pulses. To do this, we measured the precision by computing the difference profile (Fig. 5(f)) in the same way as before, but used a CCD camera to integrate 1000 patterns generated by the AOL over a frame time (30 ms). After each 30 ms, the fourth-order phase components for the AODs were incremented by $1/500^{\text{th}}$ of a wave, starting from $-1/25^{\text{th}}$ of a wave and going up to $+1/25^{\text{th}}$ of a wave. When we plotted intensity against waves of aberration (Fig. 5(g)), we found that the precision of each 1.5 Hz set of measurements (black circles) was better than $1/500^{\text{th}}$ of a wave. Further averaging over each of the 41 repeated sets of 300 measurements taken over one hour (red line) shows a precision of better than $1/1000^{\text{th}}$ of a wave. These measurements show that the physical processes involved with generating the AOL wavefront have remarkably low drift as well as high precision.

3.3. Extension of Fourier model to 3D for 4 and 6-AOD AOLs

Since one of our main motivations for developing AOL-based wavefront shaping is to correct for aberrations during AOL-based 3D microscopy, we examined whether our results could be generalised to 3D by extending our modelling. To model the correction of spherical aberration in 3D by spherical AOLs, 2D angular spectrum Fourier optic methods were used [14], a generalisation of those in Section 2.2. The Gaussian input beam waist parameter was 5.6 mm and the acoustic phase of each AOD was imposed onto the optical wavefront for the chosen instant of time ($t = 0$). To account for spatial chromatic dispersion, multiple optical wavelengths were used, weighted to fit 140 fs laser pulses. In order to keep as close as possible to the experimentally verified 2D case, we introduced spherical aberration before relaying the beam through a 0.8 magnification 4f optical system (modelled as a scaling of the wave) to the back aperture of an idealized infinity-corrected 20× water-immersion objective lens (NA $\simeq$ 0.7). This arrangement is equivalent to the case where the aberration is introduced by the objective lens and has

the benefit of being simpler to model. The angular spectrum in the natural focal plane of the objective was propagated to calculate the 3D optical field around the focal position.

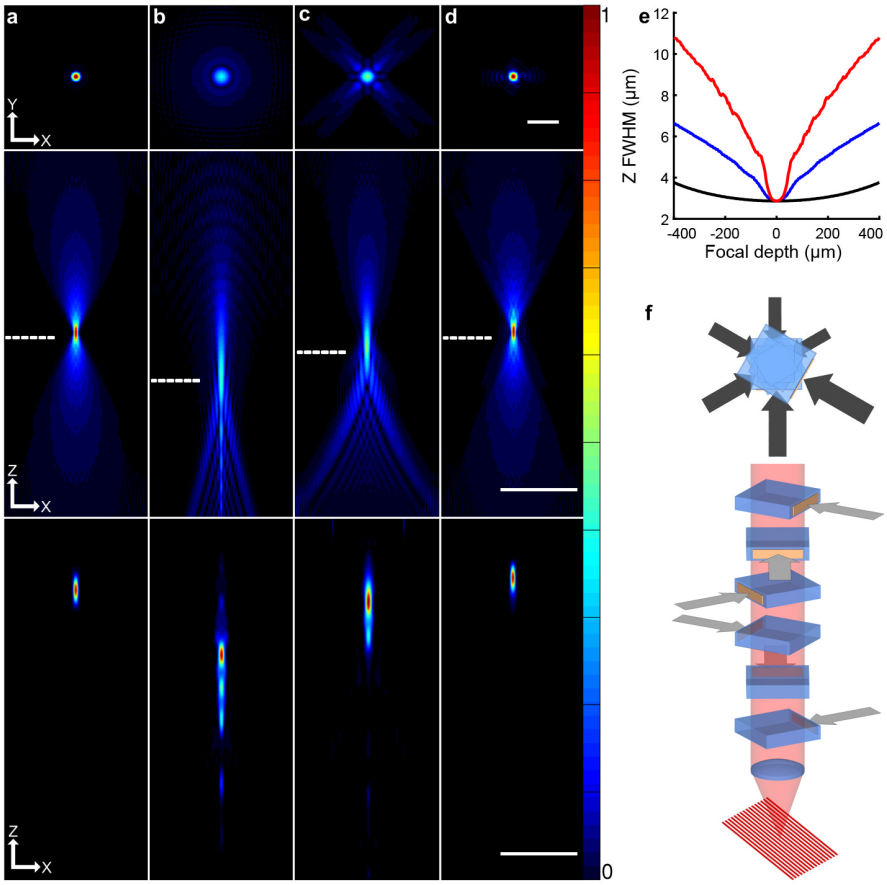

Fig. 6. Model comparing effectiveness of 4-AOD and 6-AOD AOLs at correcting spherical aberration. (a–d) Calculated using Fourier model described in Section 3.3, top: *xy* amplitude profile at location indicated by dashed lines in middle panel, middle: *xz* amplitude profile, bottom: *xz* two-photon profile. (a) Focus without spherical aberration. (b) Focus with spherical aberration. (c) Attempted correction of spherical aberration using (standard) 4-AOD AOL. (d) Correction of spherical aberration using 6-AOD AOL. Scale bars from top to bottom: 1 μm, 5 μm, 5 μm. (e) Relationship between FWHM of two-photon excitation in *xz* plane and axial defocus introduced, for uncorrected (red), 4-AOD AOL-correction (blue) and 6-AOD AOL-correction (black). (f) Top: direction of acoustic waves in 6-AOD AOL; bottom: diagram of 6-AOD AOL and spherical lens controlling an optical beam.

Figure 6(a) shows the predicted *xy* and *xz* amplitude profiles of an optical field free from spherical aberration, together with the *xz* two-photon profile below. Figure 6(b) shows how the amplitude field is altered when 10 waves of spherical aberration were added to the simulation. When $P_4 = 5$ waves were applied across each of the four AODs in a conventional AOL, part of the spherical aberration could be compensated for, producing a higher amplitude at the focal spot (Fig. 6(c)). Examination of the *xy*-projection revealed that a weak quatrefoil aberration remained, due to the inability of orthogonally arranged AODs to generate cross terms, as discussed in [10]. Nevertheless, the 4-AOD AOL could compensate for 50% of the axial elongation

of the two-photon profile induced by aberrations over a focal range of ± 400 μm at NA = 0.7 (Fig. 6(c,e)). Interestingly, applying the model to a new AOL design consisting of six AODs oriented in increments of 60^{o} (Fig. 6(f)), showed almost complete compensation over the focal range. In order to compensate 10 waves of spherical aberration, corresponding to ± 375 μm of defocus, we required 4.7 waves of fourth-order acoustic phase per AOD (Fig. 6(d,e)). The capacity to correct spherical aberration means that a 6-AOD AOL microscope has the potential to image at high spatial resolution over a larger axial range than existing AOL microscopes. A natural concern may be that the 6-AOD will be too inefficient to operate effectively. Our modelling (not described in this paper) indicates a 6-AOD could reach 15% efficiency, which is more than sufficient for biological imaging using a commercially-available high-powered laser (> 5 W).

4. Discussion

We have investigated how AOLs driven with non-linearly chirped frequencies can be used to control optical wavefronts at high-speed. Using a rapid and precise, custom-designed FPGA control system to drive a cylindrical AOL, we experimentally demonstrate aberration-free continuous axial line scanning and 2D-spherical-like aberration correction for periods of 1-10 μs at 30 kHz rates. Our experiments confirmed our AOL drive theory, which predicted the wavefront shaping that can be performed by AOLs (Table 1). Furthermore, we developed a 3D model that predicts a spherical AOL consisting of four AODs can partially correct spherical aberration, whilst a new AOL design consisting of six AODs can fully correct spherical aberration. In addition to random access pointing and lateral scanning already used in 3D two-photon AOL microscopes, the realization of axial scanning and spherical aberration correction will significantly improve their performance.

Our demonstration of *xz* line scanning and aberration correction using a cylindrical AOL shows that counter-propagating non-linearly chirped acoustic waves can be used to achieve precise optical wavefront control at unprecedented speed. This extends previous approaches that have used the brief duration of individual laser pulses to 'freeze' acoustic waveforms at a particular instant of time as they cross AODs. In contrast to this single-pulse stroboscopic approach, which restricts voxel acquisition to 40–80 kHz for high-resolution imaging [9, 10] our approach enables wavefront shaping for 1–10 μs, allowing high-speed AOL-based laser scanning with conventional femtosecond lasers (80 MHz). This reduces the time to acquire each voxel from 12.5 μs with the single-pulse strobed approach [9, 10] to as little as 0.05 μs during high-speed AOL line scanning. This has important implications for the time required to acquire full frame images and volumes. Our microscope data acquisition system samples data at 200 MHz, and imaging using lateral scans can be performed with voxel dwell times down to 50 ns. Although, the AOL is not synchronised to the laser pulses (80 MHz), averaging can be used to reduce noise when imaging at such high speeds.

Early pioneering work by Kaplan and colleagues showed that focusing can be achieved with a cylindrical AOL using sinusoidally varying acoustic drive frequencies, but fast oscillations induced significant optical aberrations, limiting the practical utility of this approach [1]. Here we show that when non-linearly chirped acoustic waves are constructed from a specific power series [Eqs. (2)], high-speed aberration-free focusing can be achieved with AOLs. This is possible because higher order optical aberrations are perfectly cancelled out by destructive interference, as the two counter-propagating acoustic waves propagate across the crystals. The ability to summate different wavefront shaping modes, including continuous axial and lateral scanning, has important applications in 3D two-photon AOL microscopy, since it enables line scanning in any direction at high speed (e.g. 20 kHz) and the scan can be aligned to match biological structures, such as dendrites which often project through multiple *xy*-planes.

Our AOL drive theory predicts that it is also possible to perform parabolic xz-scans either by acceleration in the x-direction with third-order phase components or z-direction with fourth-order phase components. It should be noted, however, that aberration will be produced by driving the AODs with same-sign fourth-order phase components (Table 1). Further investigation is needed to examine whether the aberrations produced are sufficiently small for practical use. If aberrations are modest, high-speed continuous parabolic scanning could be used to scan the curved surfaces of biological features, such as the plasma membrane of a neuron, at high-speed. This would have important applications including imaging of voltage dye reporters and photostimulation of optogenetic transducers, both of which are located in the plasma membrane.

Our experimental demonstration that a cylindrical AOL can correct for fixed aberrations introduced by cylindrical lenses establishes that AOLs can be used for high speed aberration correction. This has important implications, because spherical aberration arises in AOL microscopes when the AOL is used to focus away from the natural focal plane of the microscope objective. This is a significant current limitation of AOL-based, 3D microscopy when compared to spherical-aberration-corrected mechanical scanning designs [15], because adaptive optics devices, which could be used to correct for the spherical aberration, are too slow to operate at the 30–50 kHz required for AOL-based 3D RAPS.

We estimate that up to 4 waves of spherical aberration correction is needed for remote focusing, over an axial range of ± 150 μm with an idealized $20\times$ water-immersion objective lens. Our experimental results with cylindrical AOLs and our models of aberration correction with spherical AOLs suggest that AOL-based wavefront shaping could be used to improve the spatial resolution of 3D AOL microscopy. Although a conventional spherical AOL (which consists of four AODs) cannot fully correct for spherical aberrations due to the inability to cancel cross-terms, the partial correction that can be achieved reduces the focus-dependent axial extension of the two-photon profile by 50%. At ± 150 μm, this means the FWHM is reduced from 7 to 4.5 μm, keeping the axial FWHM between 3–4.5 μm over a 300 μm axial range. Given that small neurons have cell bodies of ~ 10 μm diameter, the reduction in axial two-photon PSF using a 4-AOD AOL will reduce fluorescence contamination from tissue above and below the region of interest.

For complete correction of spherical aberration whilst maintaining the ability to scan, our models show that a novel AOL design consisting of six AODs is required. In theory, a 6-AOD AOL can correct the first eight Zernike modes and is able to scan at high speed as well as point. However, this design is considerably more complex, and the non-orthogonal AOD arrangement makes the drive equations [2] difficult to compute. A recently proposed arrangement of four AODs oriented in 45^{o} increments [10] could correct spherical aberration and all but one of the first twelve Zernike modes. However, unlike AOLs using counter-propagating acoustic waves, it operates in the single-pulse stroboscopic mode and cannot perform high-speed scans.

Our results suggest that AOLs can perform a range of different low order wavefront shaping operations with update rates of 30–50 kHz. Unlike other wavefront shaping devices, AOLs are intrinsically discontinuous, with the wavefront only being corrected for a few microseconds before requiring a break equal to the AOD fill time to refresh. However, our results show that they are highly precise: our FPGA-based synthesizer, which updates the frequency and amplitude of the RF drive waveform every 3.3 ns, enables phase control precision of $1/35^{\text{th}}$ of a wave (note that earlier reports of $1/10^{\text{th}}$ of a wave precision [10] used a different measurement method and drive electronics which updates frequency only every 71 ns). Although, only a subset of Zernike modes can be corrected with AOLs, with the number depending on their configuration, we show that they can compensate for large numbers of waves of aberration. Indeed, our experimental results with a cylindrical AOL show that 26 waves of spherical-like aberration can be generated.

How do these properties compare to spatial light modulators (SLMs) [16] and deformable mico-mirrors (DMMs) [17]? The major advantages of AOLs compared to other devices is their precision and speed, which is 30–100 times faster than existing nematic liquid crystal on silicon (LCOS) SLMs [18]. The fastest commercially available DMMs [19] respond to drive signals at up to 64 kHz. However, there is a steep inverse relationship between update rate and stroke as a result of the inertia of the mirrors. This would result in 1.5 waves of correction at 10 kHz and 0.25 waves at 60 kHz. Moreover, studies of similar devices suggest that mirror inertia and air damping effects make control of wavefronts at high speed complex at speeds above 10 kHz [20]. While DMMs can deliver a wider range of aberrations than AOLs, it is clear that the AOL can generate considerably larger low-order corrections at high rates without the complications of inertial or damping effects. AOL-based wavefront shaping is therefore suitable for ultra-high-speed high-precision applications that only require the generation low-order Zernike modes.

The most immediate application of AOL-based wavefront shaping is to enable AOLs to perform continuous, high-speed scanning in the axial dimension. The second most important application is to partially correct for the distortions of the optical wavefront introduced by AOL-based remote focusing. However, there are also other potential applications for AOL-based wavefront shaping. As discussed in [10], AODs could also be used to correct for the aberrations introduced by the often tilted surface of the brain and the structure of brain tissue [21]. Indeed, combining the 30 kHz update rate of an AOL with the modal method of adaptive aberration correction [22] would enable low-order compensation to be achieved in a much shorter time than previously possible. The inability to generate oblique astigmatism and fully compensate for spherical aberration would limit the corrections that a 4-AOD AOLs can make. However, the 6-AOD AOL design we propose here could correct for the eight lowest-order Zernike modes, including vertical and horizontal coma and oblique astigmatism. By correcting aberrations introduced by the 3D AOL microscope and brain tissue, such systems would substantially improve the spatial resolution over the imaging volume, enabling improved functional measurements from small structures such as presynaptic boutons and dendritic spines. AOLs that implement high-speed pointing, scanning and wavefront shaping are also likely to have applications in other areas. These include optical tweezers [23], microfabrication [24, 25], data storage [26], cold atom physics [27] and enhanced resolution microscopies [28–30].

Acknowledgments

This work was funded by the ERC (294667) and the Wellcome Trust. RAS is in receipt of a Wellcome Trust Principal Research Fellowship in Basic Biomedical Science (095667). GK and VG were supported by UK EPSRC research studentships and GJE by the UCL impact PhD programme. We thank Duncan Farquharson and Alan Hogben for mechanical engineering; Jason Rothman and Bóris Marin for comments on the manuscript; and Jonathan Ashmore and Martin Booth for their comments on an earlier version of the manuscript.